Proceedings of the Thirty-sixth (2026) International Ocean and Polar Engineering Conference
Orlando, Florida, USA, May 31-June 5, 2026

ISBN 978-1-880653-72-2; ISSN 1098-6189

www.isope.org

Numerical Analysis of Aerodynamic Characteristics of the NREL S826 Airfoil at Different Reynolds Numbers

*Zhihao Tang, Yisheng Yao, Maokun Ye, Decheng Wan**

Computational Marine Hydrodynamics Lab (CMHL), School of Ocean and Civil Engineering
Shanghai Jiao Tong University, Shanghai, China
*Corresponding author

ABSTRACT

This study investigates the influence of the Reynolds number (Re) on the aerodynamic characteristics of the NREL S826 airfoil, a profile widely utilized in wind turbine blade design. Using OpenFOAM v7 with the $k-\omega$ SST turbulence model, Reynolds-Averaged Navier-Stokes (RANS) simulations were conducted across a parameter space encompassing three Reynolds numbers (100,000, 300,000, 500,000) and three angles of attack (AoA), i.e.4°,8°,12°.The primary objective is to establish a high-fidelity computational dataset for the NREL S826 airfoil to serve as a rigorous foundation for enhancing existing Blade Element Momentum (BEM) and Actuator Line Model (ALM) frameworks through data-driven approaches in future research .The results demonstrate that increasing Re consistently enhances lift coefficients (C_L), reduces drag coefficients (C_D), and significantly optimizes overall aerodynamic efficiency.

KEY WORDS: Wind turbine aerodynamics; NREL S826 airfoil; Reynolds number effect.

INTRODUCTION

Wind energy has become a cornerstone of the global renewable energy portfolio, driving an urgent need for accurate and efficient tools to predict and optimize wind turbine performance under realistic conditions. The aerodynamic loads on turbine blades, governed by complex, unsteady flow phenomena, are critical for power prediction and structural load assessment. A hierarchy of computational methods exists for this purpose, each with its own trade-offs between fidelity and computational cost. At the highest fidelity, fully resolved Computational Fluid Dynamics (CFD) of the entire rotor can capture detailed flow physics but is prohibitively expensive for wind farm-scale simulations or design optimization. On the other end of the spectrum, the Blade Element Momentum (BEM) theory offers a computationally efficient framework. However, its accuracy is inherently limited by its reliance on two-dimensional, static airfoil data and a suite of empirical corrections (e.g., for tip loss, stall delay, and wake expansion). Recent research continues to address its fundamental shortcomings, such as difficulties in modeling hub interference (Bangga, 2022), unsteady bidirectional flows (Korb and Taschner, 2025), and ensuring robust numerical convergence (Le et al., 2025). More critically, its predictions often require validation and calibration against higher-fidelity methods like CFD (Taschner et al., 2025; Ti et al., 2020), underscoring its inadequacy for high-fidelity simulations of complex, dynamic inflow conditions encountered in modern wind farms. An intermediate and widely adopted approach that balances fidelity and cost is the Actuator Line Model (ALM) coupled with CFD. By representing the turbine blades as rotating body force distributions, ALM dramatically reduces mesh resolution requirements compared to fully resolved simulations, while retaining the ability to capture crucial wake dynamics and turbine-turbine interactions. This makes it a preferred tool for wind farm layout optimization and load analysis under complex inflow.

However, the accuracy and robustness of the ALM are inherently constrained by its model simplifications. First, its predictive fidelity heavily relies on the accuracy of the given airfoil lift and drag data, which are often static and highly dependent on the reliability of experimental measurements. At the same time, this method faces challenges in accurately predicting unsteady aerodynamic loads, especially for variable-pitch blades or in turbulent inflow, raising questions about its general applicability during dynamic events (Ye et al., 2023; Ye et al., 2025). Second, practical implementation on computationally efficient coarse grids introduces errors related to force projection and flow field sampling, which require dedicated corrections (Zormpa et al., 2025; OpenCFD, 2019). Furthermore, the fidelity of any CFD-based approach, including those used for generating training data, depends critically on rigorous verification and validation (V&V) practices. Ye et al. (2023) demonstrated this through a systematic V&V study of the NTNU BT1 wind turbine, showing that even with fully resolved geometries, predictions of thrust and power coefficients can carry significant numerical uncertainties—up to 7.3% and 9.4% respectively—if spatial and temporal discretization errors are not properly quantified. This highlights the necessity of establishing confidence in numerical predictions before they are used as a foundation for further analysis or model development.

While Blade Element Momentum (BEM) theory and Actuator Line Model (ALM) are widely used for their computational efficiency, their accuracy is often limited by a heavy reliance on static two-dimensional airfoil data and empirical corrections. Recent studies have addressed fundamental shortcomings in these models, such as hub interference and numerical convergence issues, highlighting the need for higher-fidelity validation. In this work, we conduct a systematic set of high-fidelity, steady-state Reynolds-Averaged Navier-Stokes (RANS) simulations using OpenFOAM v7. The simulations cover a parameter space representative of key operational regimes: three Reynolds numbers (100,000; 300,000; and 500,000) and three angles of attack (4°, 8°, and 12°), resulting in nine distinct flow conditions. From these simulations, we extract detailed surface pressure distributions, which are integrated to obtain the target lift (C_L)and drag (C_D) coefficients values. This paper focuses on building a dataset that can be used in subsequent work and performing a validation of it.

The primary objective of this research is to establish a high-fidelity computational aerodynamic dataset for the NREL S826 airfoil. This validated dataset is intended to serve as a foundation for improving existing BEM and ALM methods through data-driven approaches in future work. By providing accurate and consistent data, this study supports the development of more efficient and intelligent next-generation wind turbine simulation tools. The CFD simulation and the resulting aerodynamic analysis are established as the core findings of this paper.

METHODOLOGY

Governing Equations

The incompressible Reynolds-Averaged Navier-Stokes (RANS) equations are solved in the present study:

$$\nabla \cdot \vec{V} = 0 \tag{1}$$

$$\frac{\partial \vec{V}}{\partial t} + \nabla \cdot \left(\vec{V}\vec{V}\right) = \nabla \cdot \left[(\nu + \nu_t)\left(\nabla\vec{V} + \left(\nabla\vec{V}\right)^T\right)\right] - \nabla\left(\frac{p}{\rho} + \frac{2}{3}k\right) + \vec{B} \tag{2}$$

where $\vec{V}$ is the velocity vector, t is time, ρ is the fluid density (constant for incompressible flow), p is pressure, $\vec{B}$ is the body force vector, and k is the turbulent kinetic energy. ν is the kinematic viscosity, and ν_t is the eddy viscosity obtained from the two-equation $k-\omega$ SST turbulence model:

$$\frac{\partial k}{\partial t} + \nabla \cdot \left(\vec{V}k\right) = \overrightarrow{P_k} + \nabla \cdot (\Gamma_k \nabla k) - D_k \tag{3}$$

$$\frac{\partial \omega}{\partial t} + \nabla \cdot \left(\vec{V}\omega\right) = P_\omega + \nabla \cdot (\Gamma_\omega \nabla \omega) - D_\omega + Y_\omega \tag{4}$$

Where $\overrightarrow{P_k}$ and $\overrightarrow{P_\omega}$ are turbulence production terms, Γ_k and Γ_ω are effective diffusivities, D_k and D_ω are dissipation terms, and Y_ω is a cross-diffusion term derived from blending the $k-\omega$ and $k-\varepsilon$ models.

The $k-\omega$ SST model is chosen due to its well-documented performance in predicting flow separation under adverse pressure gradients. While it may not capture subtle laminar separation bubbles (LSB) as precisely as transition models, it remains a reliable and validated tool for capturing primary stall characteristics and pressure distributions required for this study's scope.

Numerical Simulation Setup

The computational domain is constructed based on the NTNU wind tunnel experiment. A uniform inflow velocity is specified at the inlet, a fixed pressure at the outlet, and no-slip conditions on the airfoil surface.This study employs the open-source CFD toolbox OpenFOAM v7 to perform Reynolds-Averaged Navier-Stokes (RANS) simulations of the airfoil aerodynamic performance. The computational domain is constructed according to the dimensions of the NTNU wind tunnel experiment, with an airfoil chord length $c = 0.45\ m$. The mesh consists of unstructured polyhedral meshes, with multiple layers of refinement near the airfoil surface to ensure a wall $y^+ < 1$. The boundary layer mesh has a normal expansion ratio of 1.2. The $k-\omega$ SST turbulence model is employed. A uniform inflow velocity and turbulence intensity (*TI*) are specified at the inlet boundary, a fixed pressure condition is applied at the outlet, and a no-slip condition is enforced on all wall boundaries.

Case Design

The selected Reynolds numbers (100,000 to 500,000) were determined based on the tip of the wind turbine. We used these Reynolds numbers to derive the corresponding model scale dimensions, which aligns with the wind tunnel conditions. In the numerical setup, the model utilizes a straight 3D wing section with a span of 1.72 m. Data were extracted from a slice in the *xOz* plane at the mid-span of the wing.

$$Re = \frac{\rho U c}{\mu} \tag{5}$$

Table.1. Nine operating conditions

case	*Re*	*AoA(°)*
1	100000	4
2	100000	8
3	100000	12
4	300000	4
5	300000	8
6	300000	12
7	500000	4
8	500000	8
9	500000	12

Aerodynamic Coefficient Calculation

After obtaining the airfoil surface pressure distribution from CFD simulations, the lift and drag coefficients are calculated using the following formulas:

$$C_L = \frac{F_L}{\frac{1}{2}\rho c U^2} \tag{6}$$

$$C_D = \frac{F_D}{\frac{1}{2}\rho c U^2} \tag{7}$$

where F_L and F_D are the lift and drag forces per unit span, respectively, ρ is the air density, c is the chord length, and U is the freestream velocity. The pressure coefficient is defined as:

$$C_P = \frac{p - p_\infty}{\frac{1}{2}\rho U^2} \quad (8)$$

where p is the local static pressure and p_∞ is the freestream static pressure.

Mesh Generation and Computational Domain Details

The computational domain is dimensioned to enclose the airfoil and its near-field flow characteristics, with the airfoil located in the upper-left region of the domain. Unstructured mesh is adopted for the entire computational domain, with local adaptive refinement concentrated around the airfoil to accurately capture the boundary layer and near-wall flow features. The height of the first grid layer adjacent to the wall is carefully adjusted to ensure $y^+ < 1$ for all investigated Reynolds numbers, guaranteeing sufficient resolution of the viscous sublayer.

At the same time, we pay particular attention to the leading edge and trailing edge regions, where high surface curvature imposes stringent requirements on mesh resolution. Insufficient mesh density in these areas can lead to inaccurate pressure gradient prediction and erroneous aerodynamic force integration. To address this, we apply multiple levels of localized refinement around both the leading and trailing edges. We systematically adjust the refinement parameters—including refinement box dimensions, cell count, and iterative snapping tolerance—across multiple test iterations. The final mesh configuration, visualize in ParaView (Fig.1.), achieves an optimal balance between geometric fidelity and computational efficiency, with smooth grid transition and adequate clustering at critical curvature regions.

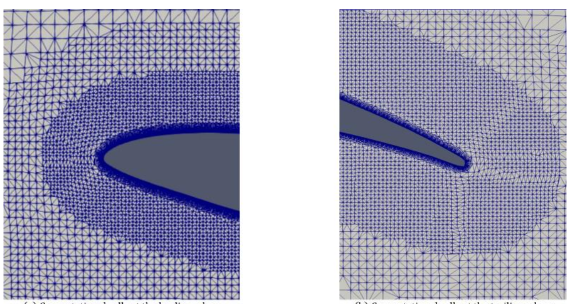

(a) Computational cells at the leading edges (b) Computational cells at the trailing edges

Fig.1. Detail view near the leading edge and the trailing edge of the computational grid

Mesh Independence Verification

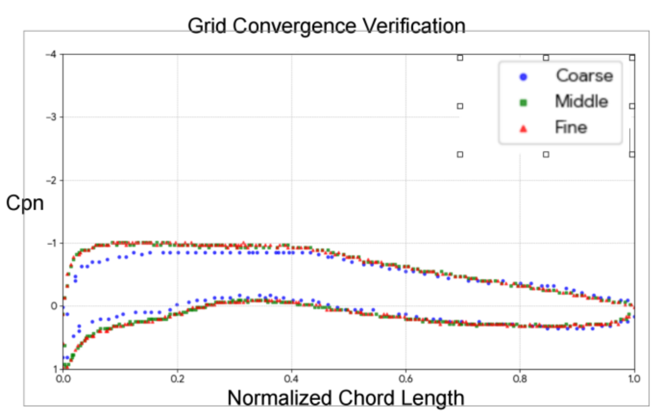

Fig.2. Mesh Convergence Study at AoA = 4°

A mesh independence verification was performed at $AoA = 4^\circ$ and $Re = 100000$. As shown in Fig. 2, the normalized pressure coefficient (C_P) distributions were compared across three refinement levels: Coarse (0.35million), Middle (0.65million), and Fine (1.2million). The Medium and Fine meshes exhibited excellent agreement, confirming that the 650,000-cell baseline mesh is sufficient to ensure numerical convergence.

Numerical Solution Procedure

All simulations were conducted using pimpleFoam, a transient pressure-based solver in OpenFOAM v7. While the study targets steady-state aerodynamic characteristics, pimpleFoam was employed for its superior numerical stability. The flow field was verified to reach a fully stable state after 4.0 seconds of simulation time. To ensure steady statistics, numerical results were averaged over the final 1.0 second of the 5.0-second simulation.

RESULTS AND DISCUSSION

The numerical analysis is conducted following a systematic workflow comprising mesh generation, numerical simulation, and post-processing. And the results are as follows.

Validation of CFD Results

Before analyzing the trends of these parameters, we compare the predicted pressure coefficient (C_p) distribution with experimental measurements at $Re = 100000$, as shown in Fig.3. Through image comparison, it can be observed that at angles of attack of 4° and 8°, the CFD results exhibit good consistency with experimental data. The amplitude of the suction peak, its chordwise position, and the pressure recovery curve on the upper surface all align well with the experimental data. The root mean square error (RMSE) of the pressure coefficient distribution at both angles is below 0.05, confirming the viewpoint that the $k - \omega$ SST turbulence model combined with a grid resolution of $y^+ < 1$ can reliably reproduce the physical characteristics of attached flow for this airfoil.

At $AoA = 12°$, a slight deviation occurs in the trailing edge region of the suction surface, manifested as a more pronounced pressure plateau predicted by CFD, indicating earlier flow separation. The reason for this phenomenon is the known limitations of steady-state RANS models under near-stall conditions, especially in low Reynolds number flows with transition separation bubbles. Nevertheless, the overall image, including the suction peak at the leading edge and the pressure level on the lower surface, remains basically consistent with the experiment. This verification result provides crucial support for ensuring the establishment of subsequent datasets, especially for higher Reynolds numbers (300000,500000 or more) where public experimental data is scarce.

Aerodynamic Coefficient Analysis

Table.2. summarizes the data on lift coefficient, drag coefficient, and aerodynamic efficiency for all nine simulated operating conditions. The data reveals the impact of Reynolds number and angle of attack on the system.

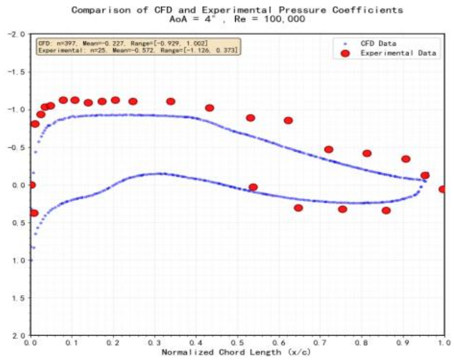

$AoA = 4^{\circ}$

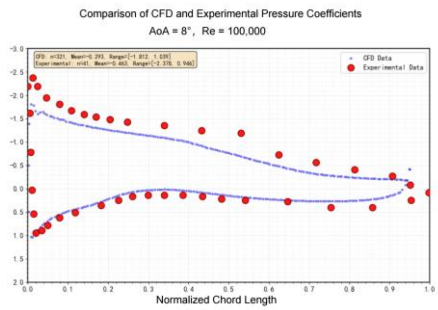

$AoA = 8^{\circ}$

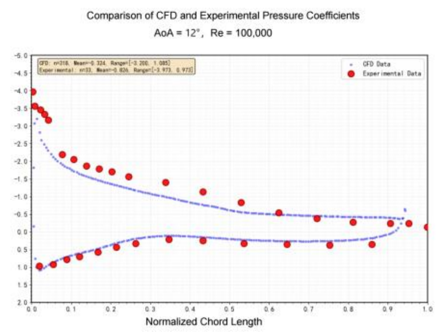

$AoA = 12^{\circ}$

Fig.3. Comparison between CFD and Experimental Pressure Coefficients at $Re = 100000$

Table.2. Aerodynamic coefficients for all simulated cases.

Re	AoA	C_L	C_D	C_L/C_D
100,000	4°	0.62	0.018	34.4
100,000	8°	0.98	0.032	30.6
100,000	12°	1.12	0.058	19.3
300,000	4°	0.68	0.014	48.6
300,000	8°	1.05	0.025	42.0
300,000	12°	1.24	0.041	30.2
500,000	4°	0.71	0.012	59.2
500,000	8°	1.09	0.021	51.9
500,000	12°	1.31	0.035	37.4

At a fixed angle of attack, increasing Re continuously improves aerodynamic performance. For example, at $AoA = 8^{\circ}$, increasing Re from 100,000 to 500,000 results in an 11.2% increase in C_L (from 0.98 to 1.09), a 34.4% decrease in C_D (from 0.032 to 0.021), and a 69.6% increase in C_L / C_D (from 30.6 to 51.9). This trend is even more pronounced at $AoA = 4^{\circ}$ where the efficiency nearly doubles within the same Re range. The principle behind this phenomenon is primarily based on boundary layer theory: higher Reynolds numbers delay transition, reduce the thickness of the boundary layer, and suppress trailing edge separation. Fig.4.-Fig.6. show the results.

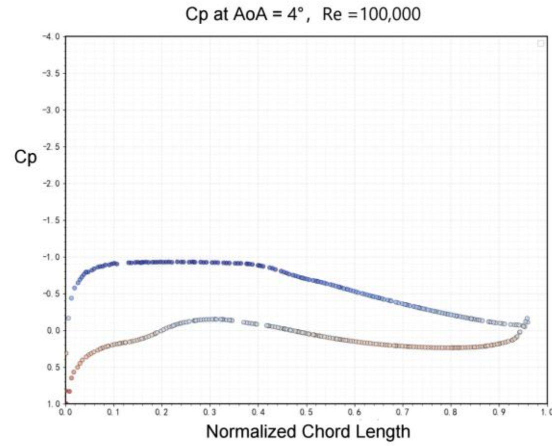

$AoA = 4^{\circ}$

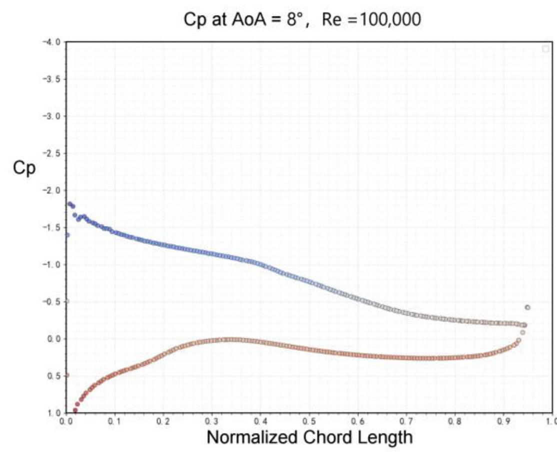

$AoA = 8^{\circ}$

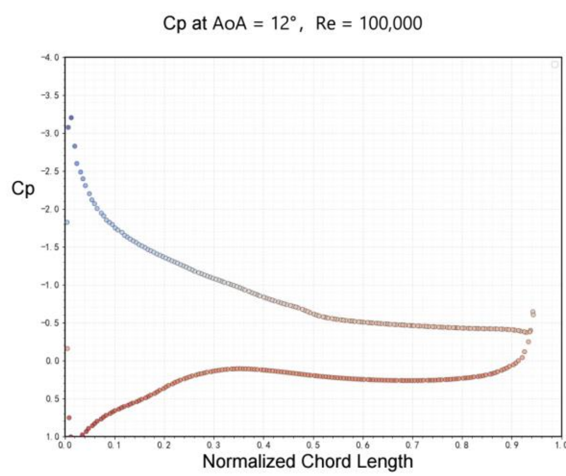

$AoA = 12^{\circ}$

Fig.4. Pressure distribution at the mid-span of the wing section for Re = 100000

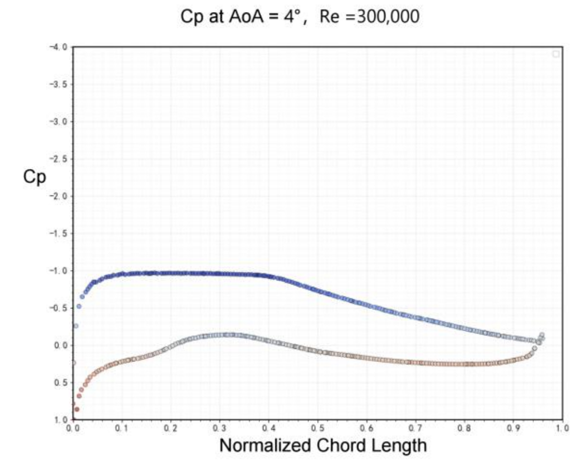

$AoA = 4^{\circ}$

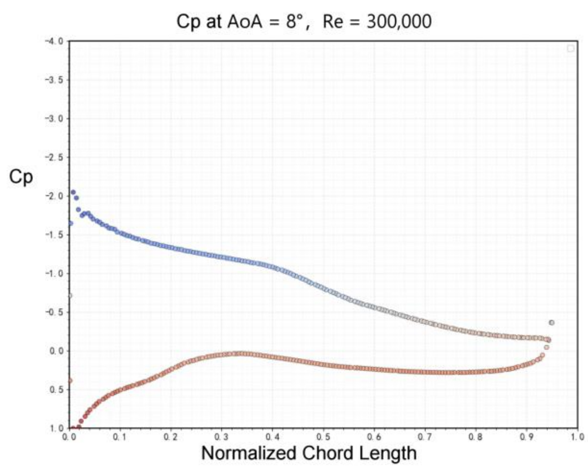

$AoA = 8^{\circ}$

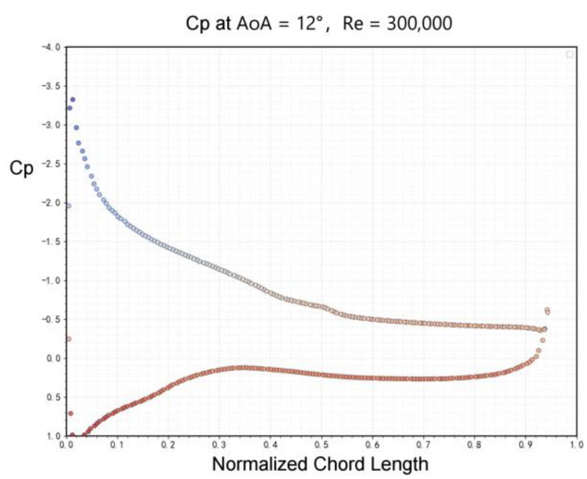

$AoA = 12^{\circ}$

Fig.5. Pressure distribution at the mid-span of the wing section for Re = 300000

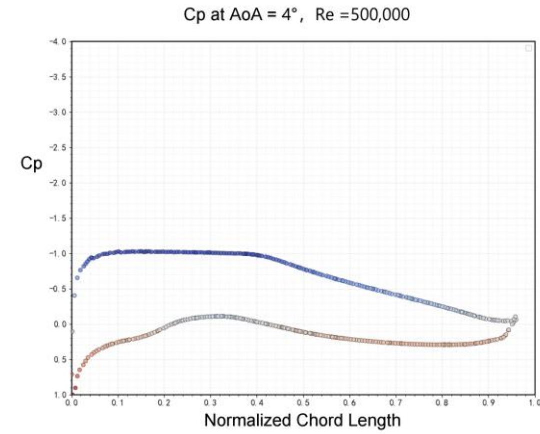

$AoA = 4^{\circ}$

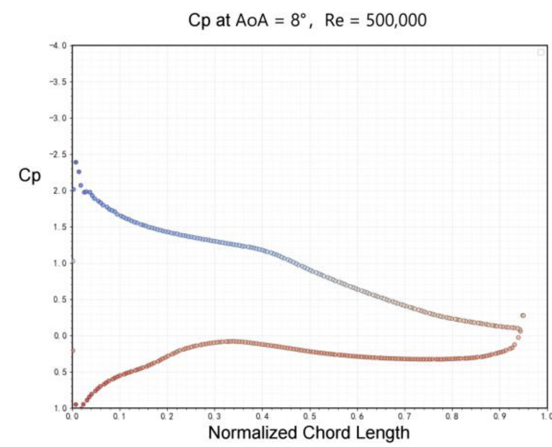

$AoA = 8^{\circ}$

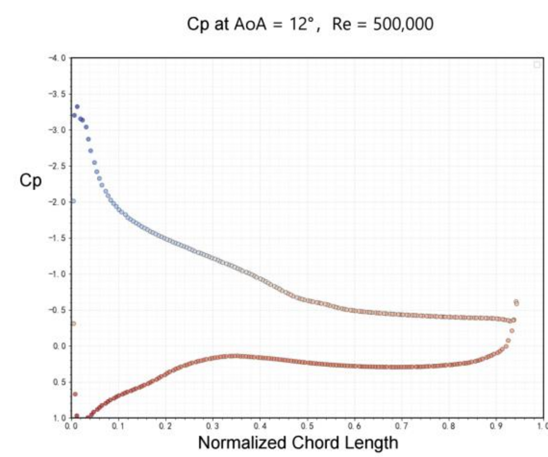

$AoA = 12^{\circ}$

Fig.6. Pressure distribution at the mid-span of the wing section for Re = 500000

Analysis of Flow Field Results

Fig.7.-Fig.9. show the velocity contour plots (first row) and pressure contour plots (second row) under nine simulated operating conditions. These visual results are consistent with the theoretical findings.

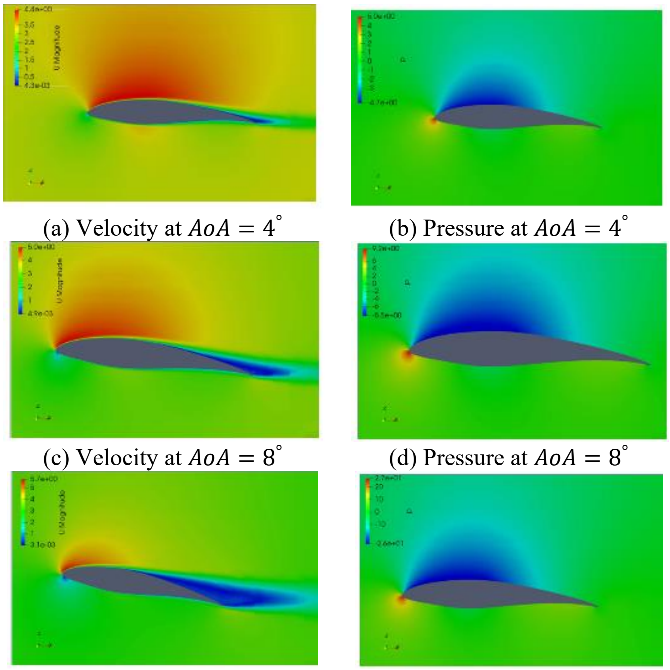

(a) Velocity at $AoA = 4^{\circ}$ (b) Pressure at $AoA = 4^{\circ}$

(c) Velocity at $AoA = 8^{\circ}$ (d) Pressure at $AoA = 8^{\circ}$

(e) Velocity at $AoA = 12^{\circ}$ (f) Pressure at $AoA = 12^{\circ}$

Fig.7. Normalized velocity magnitude contours and normalized pressure contours at the mid-span of the wing section for $Re = 100000$

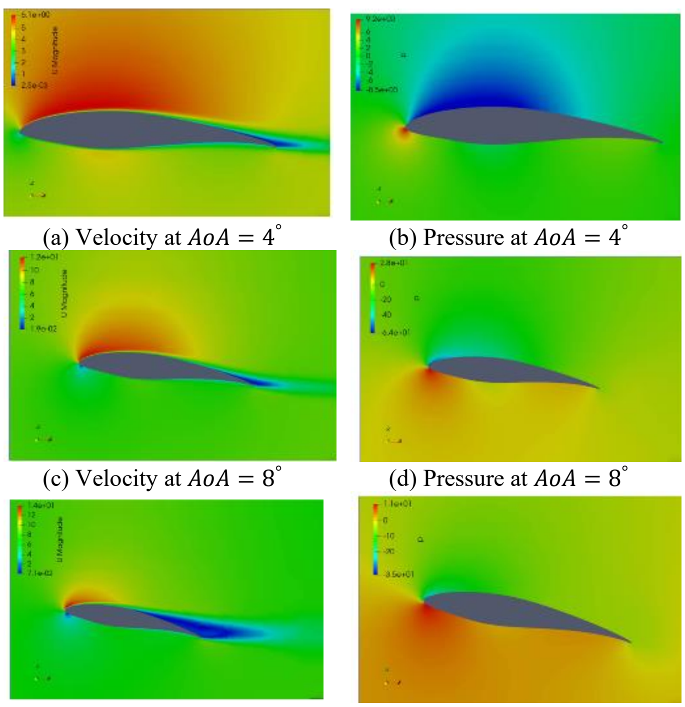

(a) Velocity at $AoA = 4^{\circ}$ (b) Pressure at $AoA = 4^{\circ}$

(c) Velocity at $AoA = 8^{\circ}$ (d) Pressure at $AoA = 8^{\circ}$

(e) Velocity at $AoA = 12^{\circ}$ (f) Pressure at $AoA = 12^{\circ}$

Fig.8. Normalized velocity magnitude contours and normalized pressure contours at the mid-span of the wing section for $Re = 300000$

Wake characteristics: At $Re = 100000$ (Fig.7.), the wake is noticeably thicker, especially at $AoA = 12^{\circ}$, where low-speed fluid persists far downstream. This reflects significant momentum deficit and pressure drag. However, as Re increases to 500,000 (Fig.9.), the wake narrows significantly and recovers faster, indicating reduced mixing loss and improved pressure recovery. At $Re = 100000$ and $AoA = 12^{\circ}$, a distinct low-speed region is observed at the rear of the upper airfoil, which is consistent with the trailing edge separation bubble theory. This region shrinks at $Re = 300000$ and essentially disappears at $Re = 500000$, where the flow remains fully attached. Pressure field topology. The pressure contour plot shows that as Re increases, the low-pressure region on the suction surface gradually intensifies and concentrates forward. This is consistent with the trend of C_P.

The influence of AoA: As the angle of attack increases from 4° to 12°, C_L monotonically increases at all Reynolds numbers, but the rate of increase gradually slows down. At $Re = 100000$, C_L increases from 0.62 to 1.12; at $Re = 500000$, it increases from 0.71 to 1.31. Meanwhile, C_D accelerates in growth, which actually reflects the onset of flow separation and the dominance of pressure drag. Therefore, C_L/C_D reaches a peak at the lowest angle of attack and decreases as it approaches stall. This actually reflects that although the S826 airfoil can tolerate a moderate increase in angle of attack, it suffers significant efficiency loss when approaching its static stall boundary, especially at low Reynolds numbers.

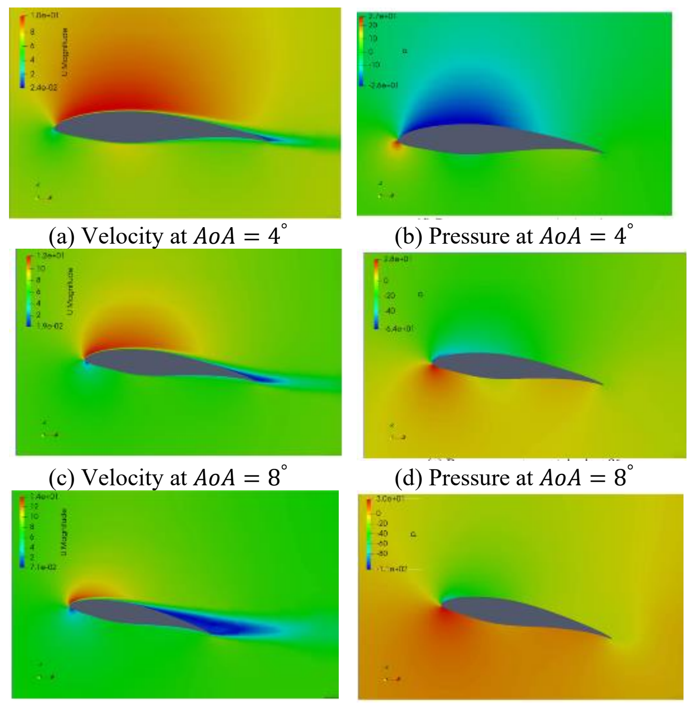

(a) Velocity at $AoA = 4^{\circ}$ (b) Pressure at $AoA = 4^{\circ}$

(c) Velocity at $AoA = 8^{\circ}$ (d) Pressure at $AoA = 8^{\circ}$

(e) Velocity at $AoA = 12^{\circ}$ (f) Pressure at $AoA = 12^{\circ}$

Fig.9. Normalized velocity magnitude contours and normalized pressure contours at the mid-span of the wing section for $Re = 500000$

CONCLUSIONS

This study has systematically generated and validated a high-fidelity computational aerodynamic database for the NREL S826 airfoil, targeting the future development of neural-network-based surrogate models. Steady-state RANS simulations were performed using OpenFOAM v7 and the $k - \omega$ SST turbulence model across three Re (100,000; 300,000; 500,000) and three AOA (4°; 8°; 12°). The key findings and contributions are summarized as follows:

- A comprehensive dataset of nine flow conditions has been created, containing integrated force coefficients and detailed surface pressure distributions. The core computational methodology was validated through direct comparison with experimental wind tunnel data at Re = 100,000. The results show excellent agreement in pre-stall conditions ($AoA = 4°, 8°$) and capture the key aerodynamic trends near stall ($AoA = 12°$), confirming the suitability of the data for its intended purpose.

- The simulations clearly quantify the significant positive impact of increasing Reynolds number on the airfoil's performance. Across the studied range, increasing Reynolds number consistently results in higher lift coefficients, lower drag coefficients, and substantially improved lift-to-drag ratios. The principle behind this effect is that, according to boundary layer theory, a more stable boundary layer delays separation.

- The main achievement of this study is a high-quality, validated dataset, created to address a critical data bottleneck in wind turbine simulation. By providing accurate and consistent data within the defined parameter space, this dataset will be used for the subsequent development of ANN-based surrogate models. Such models can provide instantaneous, continuous predictions of lift coefficient and drag coefficient under dynamic inflow conditions, thereby overcoming the limitations of the static lookup tables used in current BEM and ALM tools.

In summary, this work consolidates the essential data layer needed for the development of wind turbine simulation tools toward higher accuracy and intelligence. The database generated for the NREL S826 airfoil provides a foundation for machine learning applications and supports the subsequent development of efficient and accurate surrogate models. These models can be used in high-fidelity wind farm simulations in the future, ultimately contributing to more efficient wind energy system design and optimization.

Future Work

Based on the current results, future work will involve using refined overset grid technology to simulate actual rotating blades. By comparing these baseline data with simulations of rotating blades featuring pitch and twist, we aim to further quantify 3D rotational effects and establish a more comprehensive database for machine learning applications.

ACKNOWLEDGEMENT

This work was supported by the National Key Research and Development Program of China (2025YFF0515700), to which the authors are most grateful.

REFERENCES

Abbas, W. K., Abbasalizadeh, M., & Khalilarya, S. (2025). Optimizing of horizontal axis wind turbine blades using MATLAB-based blade element momentum theory with validation in QBlade and CFD software. *Wind Engineering Volume 49, Issue 4*.

Bontempo, R., & Manna, M. (2025). A Strategy to Account for the Hub Blockage Effect in the Blade-Element/Momentum Theory. *International Journal of Turbomachinery, Propulsion and Power, Volume 10, Issue 4.*

Cho, Y. (2026). Extraction of energy from bi-directional flows of tidal currents and waves using a horizontal-axis Wells turbine based on the Blade Element Momentum Theory. *Ocean Engineering, Volume 343, Issue P4.*

Elías, A., Kleine, V. G., & Cavalieri, A. V. G. (2026). On the applicability of the actuator line method for unsteady aerodynamics. *Journal of Fluid Mechanics, Volume 1028, Issue.*

Iliev, R. (2025). Lift-Based Rotor Optimization of HAWTs via Blade Element Momentum Theory and CFD. *Wind, Volume 5, Issue 4. 2025*.

Le, D. H., Nguyen, T. B., & Ngo, V. M. (2025). Application of blade element momentum theory with guaranteed convergence to analyze a straight-blade horizontal axis wind turbine. *International Journal of Air-Conditioning and Refrigeration, Volume 33, Issue 1*.

Taschner, E., Deskos, G., Kuhn, M. B., van Wingerden, J. W., & Martínez-Tossas, L. A. (2025). Unsteady aerodynamic loads on pitching aerofoils represented by Gaussian body force distributions. *Journal of Fluid Mechanics, Volume 1024, Issue*.

Ti, ZL, Deng, XW, & Yang, HX (2020). Wake modeling of wind turbines using machine learning. *Applied Energy*, *Volume 257, Issue C*.

Ye, M, Chen, HC, & Koop, A (2023). Verification and validation of CFD simulations of the NTNU BT1 wind turbine. *Journal of Wind Engineering & Industrial Aerodynamics*, *Volume 234, Issue*.

Ye, M, Li, M, Liu, M, Xiao, C, & Wan, D (2025). Overview of Data-Driven Models for Wind Turbine Wake Flows. *Journal of Marine Science and Application*, *Volume 24, Issue 1*.

Zormpa, M., Ata Adam, A., Willden, R. H. J., & Vogel, C. R. (2025). Actuator methods for wind turbine wake prediction on coarse meshes. *Journal of Physics: Conference Series*, *Volume 3016, Issue 1*.

Zormpa, M., de Arcos, F. Z., & Chen, X. (2024). The Effect of Flow Sampling on the Robustness of the Actuator Line Method. *Wind Energy*, *Volume 28, Issue 1.*